

Diagnosis of high-resolution upper ocean dynamics from noisy sea surface temperatures

J. Isern-Fontanet¹ and E. Hascoët²

Received 3 June 2013; revised 13 November 2013; accepted 10 December 2013.

[1] The noise present in infrared satellite measurements of sea surface temperature (SST) hampers the use of surface quasi-geostrophic (SQG) equations to diagnose ocean dynamics at high resolutions. Here we propose a methodology to reduce the contribution of noise when diagnosing surface vorticity, divergence, and vertical velocity from SST able to retain the dynamics at scales of a few kilometers. It is based on the use of denoising techniques with curvelets as basis functions and the application of a selective low-pass filters to improve the reconstruction of surface upwelling/downwelling patterns. First, it is tested using direct numerical simulations of SQG turbulence and then applied to diagnose low-frequency vertical velocity patterns from real MODIS (Moderate Resolution Imaging Spectroradiometer) images. The methodology here presented, which is not tied to the validity of SQG equations nor to the use of SST, is quite general and can be applied to a wide range of measurements and dynamical frameworks.

Citation: Isern-Fontanet, J., and E. Hascoët (2014), Diagnosis of high-resolution upper ocean dynamics from noisy sea surface temperatures, *J. Geophys. Res. Oceans*, 119, doi:10.1002/2013JC009176.

1. Introduction

[2] Infrared and visible satellite observations have revealed that the ocean surface is crowded with geostrophic eddies with scales $\mathcal{O}(10\text{--}100\text{ km})$ and submesoscale structures, like fronts and filaments, with scales $\mathcal{O}(1\text{--}10\text{ km})$. These features are known to contribute to the exchange of nutrients, heat, carbon, oxygen, and other climatically important gases between the oceanic upper layers and the ocean interior, although a precise estimation of the relative contribution of the different scales is still missing [Klein and Lapeyre, 2009]. However, during the last years, there has been growing evidence that submesoscales dominate the vertical transport in the upper few hundred meters of the ocean [Capet et al., 2008; Klein and Lapeyre, 2009], which makes these scales an important element of the coupled climate system. Nevertheless, the strong requirements in terms of spatial and temporal (~ 1 day) resolutions necessary to observe submesoscales have constrained the progress in the understanding of their dynamics and the assessment of their role in climate [Ferrari, 2011; Levy et al., 2012].

[3] Satellite infrared measurements of sea surface temperature (SST) have resolutions high enough to observe submesoscales ($\sim 1\text{ km}$), and the existence of multiple platforms with infrared sensors can provide observations of the same area with temporal samplings of less than 6 h

[e.g., Bowen et al., 2002]. Besides, the existence of long time series (>20 years) of global observations encourages to investigate possible changes in the submesoscales related to global warming. The key problem to be addressed is the extraction of quantitative dynamical information at the scales of interest from existing observations. Lapeyre and Klein [2006] and LaCasce and Mahadevan [2006] proposed that the mesoscale and submesoscale dynamics of the upper ocean layers could be modeled using an effective version of the surface quasi-geostrophic (SQG) equations, allowing to diagnose the 3-D dynamics of the ocean from a single SST image [Isern-Fontanet et al., 2006a; LaCasce and Mahadevan, 2006]. Furthermore, this approach allows to diagnose the low-frequency vertical velocities from surface data [Klein et al., 2009]. Two main limitations have to be taken into account: the existence of a phase shift between SST and the geostrophic stream function [Isern-Fontanet et al., 2008] and the presence of noise in satellite measurements.

[4] Phase shift can be reduced, in principle, by selecting SST images with the appropriate environmental conditions, but the sensitivity to noise of variables such as vorticity and surface divergence still hampers their diagnosis. Besides, the spatial requirements for the observation of submesoscales discourage the use of a low-pass filter or spatial averaging to increase the signal-to-noise ratio of satellite measurements. The problem of eliminating noise from an image without removing its finest patterns has been a major area of research in image processing during the last years [see Buades et al., 2010, and references therein]. One of the most common approaches consists in the use of nonlinear filters using wavelets as basis functions [e.g., Donoho and Johnston, 1994; Chang et al., 2000; M. Hashemi and S. Beheshti, Adaptive Bayesian denoising

¹Institut Català de Ciències del Clima, Barcelona, Spain.

²Laboratoire d'Océanographie Spatiale, Ifremer, Plouzané, France.

Corresponding author: J. Isern-Fontanet, Institut Català de Ciències del Clima, Doctor Trueta 203, ES-08005 Barcelona, Spain. (jiserf@ic3.cat)

for general Gaussian distributed (GGD) signals in wavelet domain, 2012]. The idea consists in applying the wavelet transform to the noisy image, modify the resulting wavelet coefficients, and finally, apply the inverse transform to these coefficients to recover a denoised image. During the recent years, alternatives to the wavelet transform, such as the curvelet [e.g., *Starck et al.*, 2002] and contourlet [e.g., *Cunha et al.*, 2006] transforms, have been also proposed.

[5] Here we investigate the performance of these nonlinear filters to diagnose dynamical quantities such as vorticity and surface divergence from noisy high-resolution SST observations. In particular, we have first explored existing infrared observations of the sea surface provided by the Moderate Resolution Imaging Spectroradiometer (MODIS, NASA) in order to identify the amplitude of noise and characterize their patterns. Then, the performance of a denoising algorithm based on the wavelet and curvelet transforms has been quantified using numerical experiments based on the synthetic SST fields provided by direct numerical simulations of decaying SQG turbulence.

2. Method

2.1. Surface Quasi-Geostrophic Equations

[6] The surface quasi-geostrophic equations [*Held et al.*, 1995] can be used to diagnose the stream function $\psi(\vec{x}, z)$, buoyancy $b(\vec{x}, z)$, and vertical velocity $w(\vec{x}, z)$ from a single SST $T_s(\vec{x})$ snapshot. Assuming a constant Brunt-Väisälä frequency $N(z)=N_0$, these fields are given by

$$\widehat{\psi}(\vec{k}, z) = \frac{g\alpha}{n_0\rho_0f_0} \frac{\widehat{T}_s(\vec{k})}{k} \exp(n_0kz) \quad (1)$$

$$\widehat{b}(\vec{k}, z) = -\frac{g\alpha}{\rho_0} \widehat{T}_s(\vec{k}) \exp(n_0kz) \quad (2)$$

$$\widehat{w}(\vec{k}, z) = \frac{1}{f_0^2 n_0^2} \left[J(\widehat{\psi}, b) + J(\widehat{\psi}_s, b_s) \exp(n_0kz) \right], \quad (3)$$

where z is the depth, the subindex s indicates that the field is taken at the surface, k is the modulus of the 2-D wave vector \vec{k} , $J(A, B) \equiv \partial_x A \partial_y B - \partial_y A \partial_x B$, $\widehat{\cdot}$ stands for the Fourier transform, g is the gravity, f_0 is the Coriolis parameter, ρ_0 is a reference density, $n_0 \equiv |f_0|^{-1} N_0$, and α is the thermal expansion coefficient. The application of these equations to the ocean requires to exchange the Prandtl ratio n_0 with the effective Prandtl ratio n_e to take into account the contribution of the interior potential vorticity [*Lapeyre and Klein*, 2006], and α has to be changed by α' , which is an effective thermal expansion coefficient that takes into account the partial compensation between temperature and salinity gradients when the density anomaly also depends on salinity [*Isern-Fontanet et al.*, 2008]. These parameters have to be determined with independent observations.

[7] Additional dynamical quantities such as surface vorticity $\zeta_s(\vec{x})$ and surface divergence $\partial_z w_s$ can be derived from equations (1) and (3) as

$$\widehat{\zeta}_s(\vec{k}) = -\frac{g\alpha'}{n_e\rho_0f_0} k \widehat{T}_s(\vec{k}) \quad (4)$$

and

$$\partial_z \widehat{w}_s(\vec{k}) = \frac{1}{f_0^2 n_e^2} \left[\partial_z J(\widehat{\psi}, b)_s + n_0 k J(\widehat{\psi}_s, b_s) \right]. \quad (5)$$

2.2. SST Denoising

[8] Infrared radiometers provide 2-D SST observations $T_s^{obs}(\vec{x})$ that are affected by some noise $\epsilon(\vec{x})$, i.e.,

$$T_s^{obs}(\vec{x}) = T_s(\vec{x}) + \epsilon(\vec{x}). \quad (6)$$

[9] Since noise has a stronger effect on short wavelength, a common approach consists in low-pass filter SST observations with a predefined cutoff wavelength λ_c to recover the original SST. Mathematically, this approach consists in first projecting SST onto complex exponentials, which form a base of functions of the 2-D space $\{\phi_{\vec{m}}(\vec{x})\}$, i.e.,

$$T_s^{obs}(\vec{x}) = \sum_{\vec{m}} a_{\vec{m}} \phi_{\vec{m}}(\vec{x}), \quad (7)$$

where

$$a_{\vec{m}} = \langle T_s^{obs}(\vec{x}), \phi_{\vec{m}}(\vec{x}) \rangle \quad (8)$$

is the scalar product between the SST field and each of the vectors of the base. Then, the original signal $T_s(\vec{x})$ is approximated by

$$T_s(\vec{x}) \approx \sum_{\vec{m}} b_{\vec{m}} \phi_{\vec{m}}(\vec{x}), \quad (9)$$

where the set of new coefficients $\{b_{\vec{m}}\}$ has been obtained as (although equation (10) cannot be applied directly due to the Gibbs phenomenon, the underlying idea does not change.)

$$b_{\vec{m}} \equiv \begin{cases} a_{\vec{m}} & \text{if } \lambda_{\vec{m}} \geq \lambda_c \\ 0 & \text{if } \lambda_{\vec{m}} < \lambda_c \end{cases}. \quad (10)$$

[10] Here $\lambda_{\vec{m}}$ is the characteristic wavelength associated to the base function $\phi_{\vec{m}}$ and \vec{m} is its vector of subindices, e.g., $\vec{m} = (m_x, m_y)$ for a 2-D Fourier transform. This approach has two main drawbacks: the signal at wavelengths shorter than λ_c is lost and no noise correction is done at wavelengths longer than λ_c .

[11] Alternatively, equation (9) can be applied using different base functions and selecting the new set of coefficients based on their statistical reliability rather than on a predefined wavelength. In particular,

$$b_{\vec{m}} \equiv \begin{cases} a_{\vec{m}} & \text{if } |a_{\vec{m}}| > \tau_{\vec{m}} \\ 0 & \text{if } |a_{\vec{m}}| \leq \tau_{\vec{m}} \end{cases}, \quad (11)$$

where τ_m is a threshold value given by

$$\tau_{\vec{m}} = K \sigma_{\vec{m}}^{\epsilon} \sigma_{\epsilon}. \quad (12)$$

[12] The parameter K is usually taken equal to 3 and $\sigma_{\vec{m}}^{\epsilon}$ is the correction to the noise standard deviation associated to the base function $\phi_{\vec{m}}(\vec{x})$. This approach is known as *hard-thresholding* denoising. In general, noise is assumed

to be Gaussian with a standard deviation σ_ϵ , although this is not a necessary condition and the above approach can be adapted to non-Gaussian noise [see *Starck and Murtagh, 2006*, and references therein].

[13] The success of this approach partly depends on the basis functions used. In general, the closer these functions are to the characteristic patterns of the input field, the better are the results. The most common choice are 2-D isotropic wavelets [Schneider and Farge, 2006], which are good candidates when the flow is dominated by vortices [e.g., *Turiel et al., 2007*]. However, at high resolutions the flow is crowded with anisotropic features like filaments and fronts. Consequently, other type of basis functions should be explored. Here we have explored the use of curvelets, which are a multiscale transform with strong directional characteristics in which elements are highly anisotropic at fine scales [Starck et al., 2002; Candès et al., 2006].

[14] Figure 1 shows some examples of isotropic wavelets and curvelets, which makes evident the differences between these basis functions. From Figure 1 it is also evident that one needs more indices to identify each function of the base. Indeed, the vector of indices associated to the wavelet transform when using isotropic wavelets is $\vec{m} = (m_x, m_y, m_l)$, which identifies the position of the wavelet and its scale m_l , and for the curvelet transform it is $\vec{m} = (m_x, m_y, m_l, m_\theta)$, which also specifies its orientation m_θ . Contrary to the Fourier basis, wavelets and curvelets are localized in space, which requires to specify its location in addition to its scale.

3. Procedures and Data

3.1. Method Implementation

[15] The implementation of the method described in section 2.2. using wavelets is standard and is well described in most textbooks of image processing. In addition, several libraries provide the necessary routines to apply such denoising to images. In particular, in this study we have used the stationary wavelet transform (*à trous* algorithm) [Mallat, 1999] with B_3 -splines to perform our denoising experiments as it is described in *Starck and Murtagh [2006]*. This algorithm was selected because it is a redundant transform and therefore, tends to provide better results when applied to denoising problems [e.g., *Cunha et al., 2006*]. Although curvelets are more complex objects compared to wavelets, their use is simple due to the existence of freely available libraries. In particular, we used here the fast curvelet transform [Candès et al., 2006] provided by the CurveLab 2.8.2 library (www.curvelet.org). This library provides examples of the applications of curvelets to denoising problems that can be easily adapted to remote sensing images.

[16] When noise is Gaussian, its standard deviations σ_ϵ can be automatically estimated using the *K-sigma clipping* method [e.g., *Starck and Murtagh, 2006*]. This method exploits the dominance of noise at short wavelengths. The method is as follows. A first guess of σ_ϵ is obtained from the standard deviation of a high-pass filtered version of the noisy field. Then, those values with amplitudes larger than K times σ_ϵ are rejected, and a new estimation of σ_ϵ is obtained from the standard deviation of the remaining values. This procedure is applied iteratively until σ_ϵ is obtained. Here we have used the wavelet coefficients at the

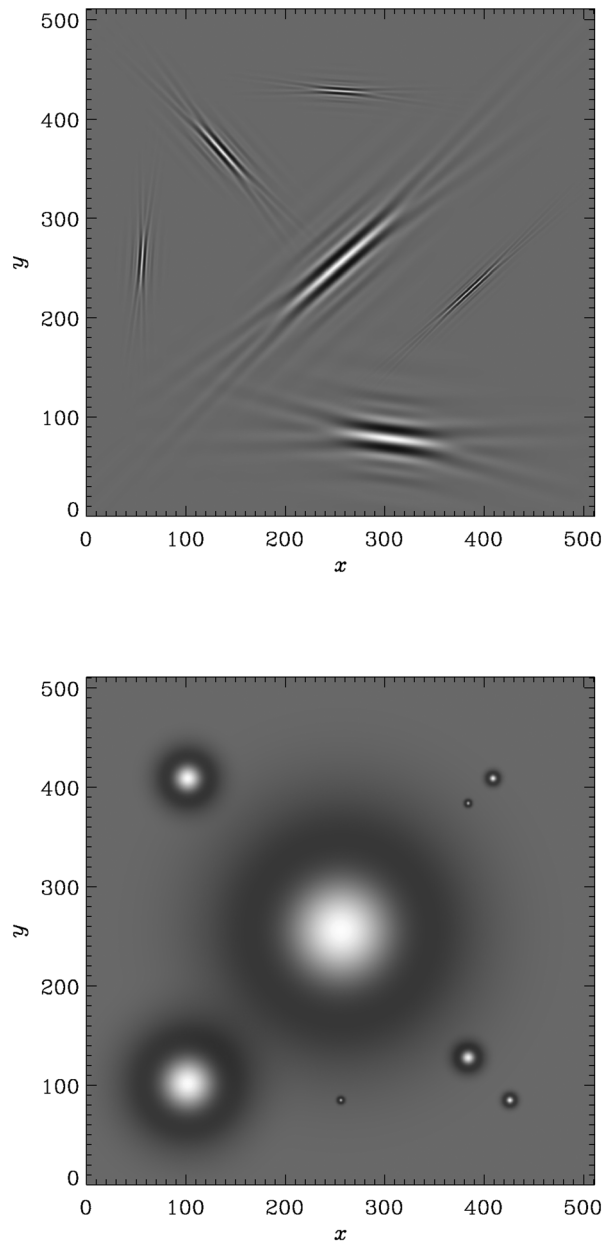


Figure 1. Example of base functions. (top) Curvelets of different scales and orientations. (bottom) B3-splines of different sizes.

shortest scales to obtain a low-pass filtered version of the noisy field, which requires to correct the contribution of the wavelet base [Starck and Murtagh, 2006].

3.2. Satellite Data

[17] Sample Level 1 MODIS-Aqua images were downloaded from the NASA's Goddard Space flight Centre (oceancolor.gsfc.nasa.gov) to explore the difficulties to diagnose the high-resolution dynamics and to have a realistic estimation of the noise level present in real observations (see Table 1). These images have a spatial resolution of 1 km at its nadir. Data were processed using SeaDAS 6.0 to obtain SST and brightness temperature (BT) from the channel centered at 11 μm . BT was actually also considered

Table 1. Noise Standard Deviation σ_ϵ and Kurtosis κ_1 of the Smallest Wavelet Coefficient Dominated by Noise Obtained From MODIS-Aqua Image Samples^a

Granule ID	i_{\min}	j_{\min}	BT		SST	
			σ_ϵ (K)	κ_1	σ_ϵ (K)	κ_1
A2002281171500	157	1223	0.05	0.69	0.12	-0.01
A2003023052500	523	1040	0.02	-0.10	0.11	-0.16
A2004027173500	691	1433	0.04	0.39	0.08	0.12
A2005122171000	48	200	0.06	0.73	0.16	-0.02
A2006311174500	463	1240	0.03	0.17	0.07	0.15
A2007218132000	345	1110	0.03	0.45	0.13	-0.05
A2007322120500	500	290	0.03	0.78	0.12	-0.09
A2009286171000	524	1195	0.04	0.41	0.15	-0.09
A2009286171000	540	398	0.04	0.62	0.11	0.07
A2009286171000	337	817	0.04	0.41	0.14	-0.05

^aSample images are identified by their granule ID and the lower left pixel (i_{\min}, j_{\min}) position of the 512×512 subimages.

since it has lower levels of noise [Bowen *et al.*, 2002; Robinson, 2004], which is evident comparing the SST and BT fields of Figure 2. Subsets of 512×512 pixels were extracted from the original image. First, the bow tie effect present in the images was corrected, and gaps due to clouds or land were filled using the same approach as in *Isern-*

Fontanet et al. [2008], which consisted in replacing missing data by a weighted average of valid points around it. Weights were proportional to the inverse of the distance. To this end we used a mask based on the cloud and land masks and on the SST quality index, which was taken to be equal or smaller than 2 [Brown and Minnett, 1999]. The mask of some of the images was manually corrected to avoid losing valid points associated to strong thermal gradients. Vertical stratification n_0 was estimated from the World Ocean Atlas 2009 climatology.

3.3. Direct Numerical Simulations of SQG Turbulence

[18] An adimensional version of the equation for the temporal evolution of SST

$$\frac{\partial T_s}{\partial t} + J(\psi_s, T_s) = 0 \quad (13)$$

and equation (1) was used in order to generate SST fields numerically. The spatial domain for the simulations was chosen to be a $2\pi \times 2\pi$ square on which periodic boundary conditions are imposed. The numerical algorithm implemented is based on a pseudo-spectral Fourier-Galerkin decomposition with a 3/2 dealiasing rule. Time integration was then performed by using a fourth-order Runge-Kutta

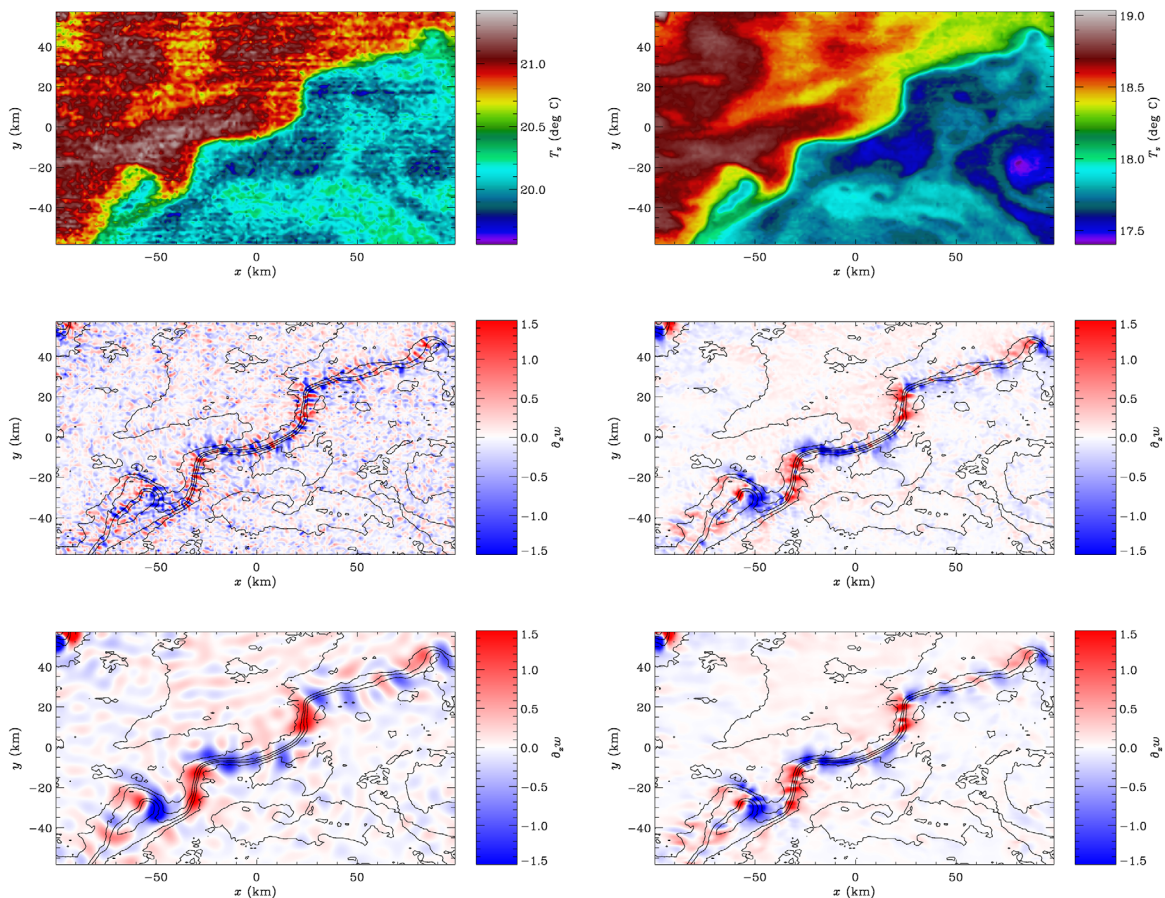


Figure 2. (top, left) SST and (top, right) BT fields in the Agulhas region provided by MODIS-Aqua on 18 November 2007. (middle) Surface divergence estimated directly from (left) SST and (right) BT fields. (bottom) Surface divergence estimated from BT applying (left) a low-pass filter with $\lambda_c = 10$ km and (right) using curvelet denoising.

method. We employed a resolution of 1024^2 Fourier modes. Since we are interested in the properties of a flow that is turbulent, we selected a random phases initial velocity field with a prescribed kinetic energy spectrum peaked at low wave numbers. In order to dissipate potential temperature variance at small scale a hyperviscous dissipation term $\nu\Delta^8 T_s$ was added into equation (13). The velocity field was then let evolve until the predicted decaying $k^{-5/3}$ power-law spectrum for the potential temperature variance cascade was approached.

[19] Figure 3 shows a SST snapshot and the associated surface vorticity and vertical velocity at 100 km. Dimensional units were recovered using a length scale, $L = 300$ km, a velocity scale, $U = 2.18$ m s⁻¹, a Coriolis parameter, $f_0 = 7.27 \times 10^{-5}$ s⁻¹, and a Brunt-Väisälä profile, $N^2 = 1.9 \times 10^{-5}$ s⁻² leading to a grid spacing of $\Delta x = \Delta y = 1.84$ km. In these simulations we did not take into account the role of salinity gradients nor interior potential vorticity (PV). Therefore, $\alpha' \equiv \alpha$, where α is the thermal expansion coefficient and $n_e = n_0$. Once scaled, numerical simulations revealed vortices with diameters ranging from 10 to 200 km and the filaments between vortices with widths between 5 and 10 km (Figure 3).

4. Results

4.1. Satellite Observations

[20] MODIS sample images were projected onto a flat surface using a local Mercator projection and were then interpolated onto a regular doubly periodic grid before equations (1–5) were applied. Results revealed that SST fields were, in general, too noisy to determine the sign of the upwelling/downwelling patterns (see the example in Figure 2). On the contrary, the noise level in BT fields was low enough to provide a qualitative picture of the dominant patterns, although the resulting divergences were still noisy. Two other difficulties were encountered when estimating surface divergence from MODIS data. First, the striping characteristic of these measurements could generate spurious upwelling/downwelling patterns. Second, mixed layer (ML) instabilities, which appeared as small patterns along ocean fronts, had associated strong divergences when they were directly diagnosed using the SQG framework (not shown). In many situations, the patterns associated to the striping could be corrected by just reordering the pixels based on their geographical coordinates. However, the removal of ML instabilities was more subtle, and consequently, we decided to discard those images that exhibited such patterns at this stage.

[21] The wavelet transform was applied to MODIS images, and the K-sigma clipping method (section 3.1.) was used to identify the noise-dominated coefficients. Their probability density functions (PDFs) were characterized by a shape close to a Gaussian distribution for SST (Figure 4), and their noise standard deviation was estimated to be between $\sigma_\epsilon = 0.06$ K and $\sigma_\epsilon = 0.17$ K (see Table 1). On the contrary, BT had lower levels of noise [e.g., Bowen *et al.*, 2002; Robinson, 2004] ranging between $\sigma_\epsilon = 0.02$ K and $\sigma_\epsilon = 0.06$ K. The shape of the PDF for BT was more variable in comparison to the PDF for SST. It ranged between a Gaussian distribution and a PDF characterized by heavier tails (compare kurtosis in Table 1 and Figure 4). Since both distributions were very similar we only considered a Gaussian distribution for the numerical experiments described in the next section.

4.2. Numerical Experiments

[22] The synthetic noise-free SST fields provided by the numerical simulations of SQG turbulence were degraded with Gaussian noise of different standard deviations ranging from $\sigma_\epsilon = 0.01$ K to $\sigma_\epsilon = 1$ K. Then, they were denoised using wavelets and curvelets. The new vorticity, divergence, and vertical velocity were diagnosed from the resulting fields and compared with the ones derived from the noise-free SST fields using linear correlation and the root-mean-square error (RMSE) as metrics.

[23] Figure 3 shows the results corresponding to $\sigma_\epsilon = 0.05$ K, which is representative of the noise level in BT images. As it can be seen, SST fields were qualitatively similar. Besides, the reconstruction of vertical velocities at 100 m was reasonably good, even when estimated directly from noisy SST fields. On the contrary, the capability to retrieve vorticity was very poor away from the strongest vorticity filaments without the application of a denoising method. The reconstruction was also difficult for surface divergence since it was not possible to determine the sign of the upwelling/downwelling patterns away from the flow patterns with larger amplitudes when noisy SST were used (not shown for this experiment). The values for the correlation and RMSE confirmed this view. On one side, the correlation for SST was as high as 0.98, while the correlations for surface vorticity and divergence were of the order of 0.2 (see Table 2). On the other side, the RMSE represented about the 20% of the RMS of SST, but the RMSE represented the 500% and 434% of the RMS for vorticity and surface divergence, respectively. The reconstruction of vertical velocities at 100 m corresponded to an intermediate situation, with spatial correlations of 0.66 and a RMSE of 114% of the original RMS.

[24] The application of the curvelet and wavelet denoising methods significantly improved the results as it is evident in Figure 3. From a qualitative point of view, the wavelet- and curvelet-denoised SSTs were very similar and it was difficult to identify the differences. On the contrary, differences between both denoising methods were more evident in the vorticity field. Indeed, wavelet-denoised vorticity still contained a significant quantity of *salt and pepper*, and vorticity filaments were patchy. Besides, curvelet-denoised vorticity field was closer to the original one, although it exhibited the scars associated to the base functions (this can be seen when Figure 3 or 7 is enlarged). Vertical velocities were qualitatively similar for both base functions. In terms of correlations, the improvement was significant (see Table 2). The correlation for vorticity increased from 0.19 to 0.72 (wavelets) and 0.9 (curvelets), and the correlation for surface divergence increased from 0.22 to 0.63 (wavelets) and 0.79 (curvelets). Correlations for vertical velocity were quite high reaching values larger than 0.9. The resulting RMSEs of the wavelet-denoised fields represented between 15% (vorticity) and 36% (SST) of the RMSE of noisy fields. The reduction of the error was even larger for the curvelet-denoised fields, and the new RMSE ranged between the 8.7% (vorticity) and 28.8% (SST) of the RMSE for noisy fields. The same analysis was applied to different time slices with similar quantitative results.

[25] The correlations and RMSE for all the experiments performed can be found in the Taylor [2001] diagrams of

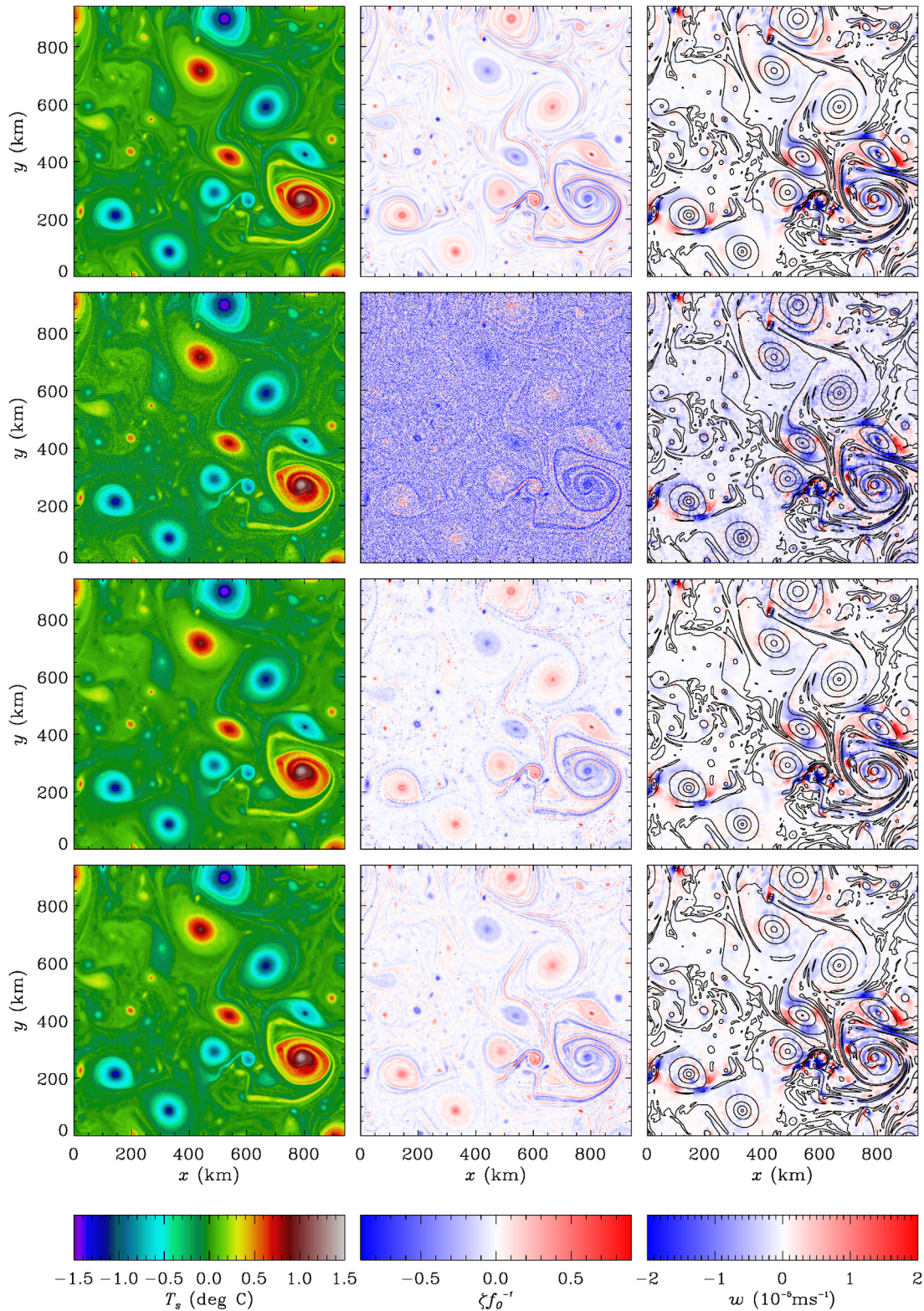


Figure 3. Numerical experiments. Columns (left to right): SST (T_s), vorticity (ζ) and vertical velocity (w) at 100 m depth derived from SST using the SQG equations. Rows (top to bottom): original fields, noisy fields with $\sigma = 0.05$ K, denoised fields using wavelets and denoised fields using curvelets.

Figures 5 and 6. As expected, RMSE increased and spatial correlation decreased as σ_ϵ became larger. Results revealed that curvelet-denoising outperforms the wavelet-denoising

here used for a wide range of noise amplitudes. Among the different experiments done, the one with $\sigma_\epsilon=0.1$ K is of particular interest since it represents the typical noise level

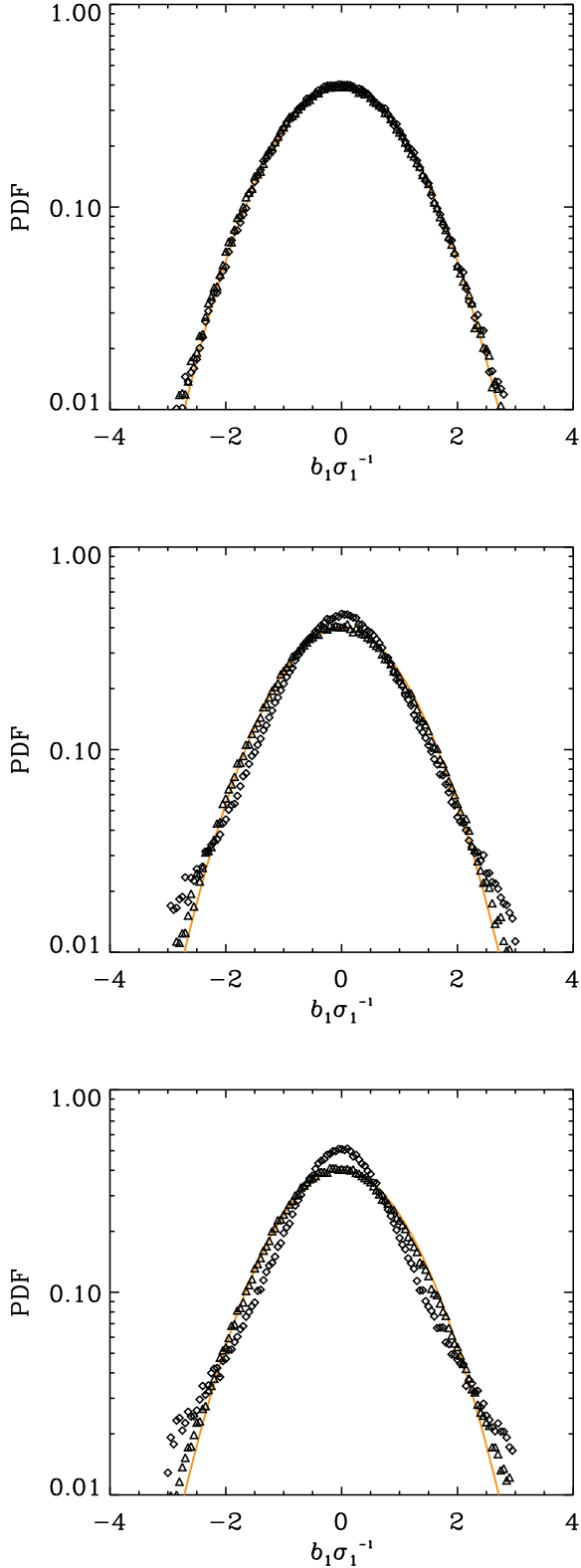


Figure 4. Sample probability density functions of the wavelet coefficients for the smallest scales selected using the K-sigma clipping method for different MODIS images. Triangle corresponds to SST and squares to BT. The solid line represents a Gaussian PDF. The subindex 1 refers to the wavelet coefficients at the smallest scale.

of SST images. In this case, results are qualitatively similar compared to the experiment with $\sigma_\epsilon=0.05\text{K}$ but the improvement in the RMSE is much larger as it is evident from Table 2. However, the RMSE are larger and correlations lower than the experiment with $\sigma_\epsilon=0.05\text{K}$. Figure 7 shows the surface divergence for this experiment. From Figure 7 the improvement due to the curvelet denoising is evident.

[26] Surface divergence, however, can still contain spurious upwelling/downwelling patterns after denoising, which is evident on the structures surrounding the vortex centered at $x = 800$ km and $y = 400$ km in Figure 7. To improve the results we explored an additional denoising strategy that we called partial filtering. It consisted in splitting the stream function computed from the denoised SST into

$$\psi_s(\vec{x}) = \psi_s^H(\vec{x}) + \psi_s^L(\vec{x}), \quad (14)$$

where $\psi_s^H(\vec{x})$ and $\psi_s^L(\vec{x})$ were, respectively, the high-pass and low-pass contributions to the stream function separated by a cutoff wavelength λ_c . Then, surface divergence was calculated from the denoised full resolution SST and the low-pass filtered stream function $\psi^L(\vec{x}, z)$, i.e.,

$$\partial_z \widehat{w}_s(\vec{k}) \approx \frac{1}{f_0^2 n_c^2} \left[\partial_z J(\widehat{\psi^L}, b)_s + n_0 k J(\widehat{\psi_s^L}, b_s) \right]. \quad (15)$$

[27] From a physical point of view, this approach implies that only the surface divergence associated to the interaction of a larger scale flow with the SST is retained. We explored a range of cutoff wavelengths from zero to $\lambda_c = 30$ km (not shown), and results showed that in our simulations, the best reconstruction was obtained with $\lambda_c \sim 15$ km, although filamentary structures were visually more continuous with higher values of λ_c . This showed that the interaction between SST and currents with wavelengths shorter than λ_c was removed reducing the amplitude of the divergences diagnosed from SST (Figures 6 and 7).

4.3. Denoising of Real Observations

[28] Curvelet denoising was applied to the sample MODIS images, and the procedure outlined in section 4.1. was used to diagnose the ocean dynamics. The qualitative inspection of surface divergences clearly revealed a significant reduction of noise in both BT (Figure 2) and SST (not shown) fields, similar to the results of the numerical experiments shown in the previous section (e.g., Figure 7). For SST fields we had to cope with an additional difficulty: some scan lines had higher/lower mean temperatures (e.g., Figure 2), which favored the alignment of curvelets along these lines and the generation of spurious cross-track divergence patterns (not shown). This makes necessary the correction of such features if the diagnosis is done using SST. In addition, the resulting divergence fields were compared with divergences obtained from the application of a low-pass filter to BT. Figure 2 shows such comparison using a low-pass filter with a cutoff wavelength $\lambda_c = 10$ km. It reveals that curvelet denoising retained smaller patterns than the low-pass filtered fields. Furthermore, away from the meandering front the low-pass filter generated some divergence/convergence patterns not observed in the divergence field derived directly from BT.

Table 2. Correlation and Root-Mean-Square Error (RMSE) Between the Different Numerical Experiments and the Original Fields^a

Denoising Method	Partial Filtering	σ_ϵ (K)	λ_c (km)	Correlation				RMSE			
				T_s	ζ_s	$\partial_z w_s$	w_{100m}	T_s (K)	ζ_s (s ⁻¹)	$\partial_z w_s$ (s ⁻¹)	w_{100m} (m s ⁻¹)
None	No	0.05	0	0.98	0.19	0.22	0.66	0.050	3.65×10^{-5}	5.36×10^{-7}	3.76×10^{-6}
Wavelet	No	0.05	0	1.00	0.72	0.63	0.95	0.018	0.55×10^{-5}	1.12×10^{-7}	0.99×10^{-6}
Curvelet	No	0.05	0	1.00	0.90	0.79	0.97	0.014	0.32×10^{-5}	0.79×10^{-7}	0.86×10^{-6}
Curvelet	Yes	0.05	30	–	–	0.76	–	–	–	0.80×10^{-7}	–
None	No	0.10	0	0.92	0.10	0.09	0.35	0.100	7.31×10^{-5}	13.6×10^{-7}	8.71×10^{-6}
Wavelet	No	0.10	0	0.99	0.54	0.43	0.89	0.027	0.75×10^{-5}	1.57×10^{-7}	1.51×10^{-6}
Curvelet	No	0.10	0	1.00	0.77	0.62	0.91	0.023	0.48×10^{-5}	1.00×10^{-7}	1.37×10^{-6}
Curvelet	Yes	0.10	30	–	–	0.67	–	–	–	0.92×10^{-7}	–

^aNoise levels are representative of MODIS BT and SST.

[29] Figure 8 shows a second example of the application of this procedure to an image in the region of the Alboran sea (western Mediterranean sea), where the northeast part of the Alboran Gyre is visible. During this part of the year, the incoming fresh Atlantic water is warmer than the resident saltier one, allowing the direct application of the SQG equations. In this image, the partial filtering strategy was used to reconstruct divergences applying a cutoff wavelength of $\lambda_c = 20$ km to the surface stream function before estimating them. As it can be seen from the image, there was a good coincidence between the maximum of chlorophyll and the area with strongest upwelling.

5. Discussion

[30] The analysis of numerical simulations and sample MODIS images has revealed that the noise level in SST is large enough to corrupt derived fields such as vorticity and surface divergence. On the contrary, vertical velocities were less affected by noise at depths of 100 m, although it is one of the most elusive variables in the ocean. An interesting characteristic of the SQG framework is that small horizontal scales have weaker penetrations than larger scales, which is evident from equations (1) and (2). Indeed, the reconstruction of subsurface dynamics from surface

fields can be seen as the application of a low-pass filter that depends on ocean stratification, which reduces the contribution of noise. Consequently, it may not be necessary to denoise the data to derive subsurface fields if the stratification is strong enough. On the contrary, without the use of denoising techniques such as the one here proposed, it would not be possible to unveil some surface high-resolution dynamical patterns. It is worth mentioning that our results showing that the curvelet-based approach is superior to the wavelet-based approach are in agreement with previous studies in image processing [e.g., Starck *et al.*, 2002].

[31] Although the use of curvelet denoising significantly improves the estimation of ocean dynamics, it is of great importance to reduce the noise level as much as possible and avoid the generation of spurious patterns due to instrument design (e.g., striping). As it has been shown, the use of BT instead of SST represents a significant improvement due to its lower levels of noise. However, BT may not be the best candidate in all conditions since the lack of atmospheric correction could induce spatial inhomogeneities at scales $\mathcal{O}(10$ km) that would impact on the diagnosed dynamics. Since larger scales are more energetic than smaller scales, the noise level affects the spatial resolution that can be accessed. The hard-thresholding approach here

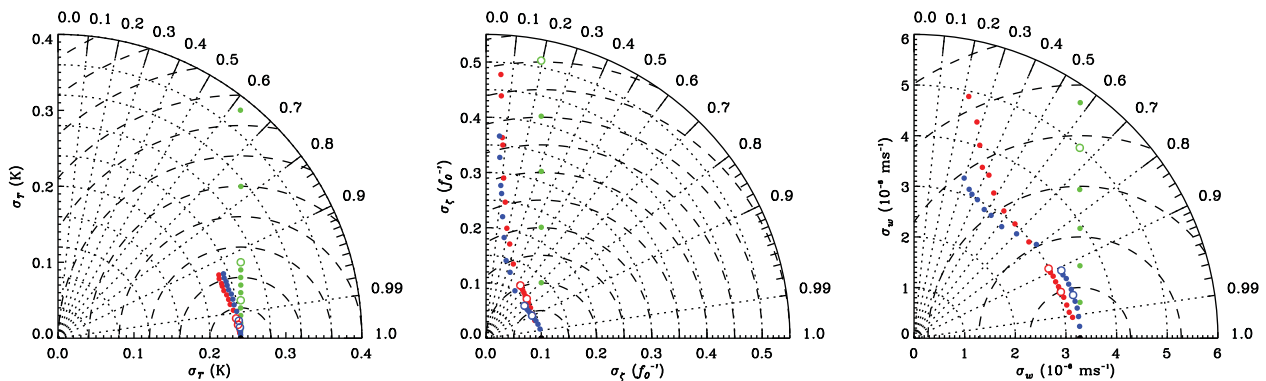


Figure 5. Taylor diagrams for the fields shown in Figure 3 comparing noisy fields (green), wavelet-denoised fields (red), and curvelet-denoised fields (blue) with the fields without noise for (left) SST, (middle) vorticity, and (right) vertical velocity at 100 m. Noise amplitude increases as the distance to the reference point (black bullet) increases. Circles correspond to the experiments with $\sigma_\epsilon = 0.05$ K and $\sigma_\epsilon = 0.1$ K reported in Table 2. Bullets corresponds to experiments with noise amplitudes increasing by 0.01 K for the range between 0 and 0.1 K and by 0.1 K between 0.1 and 1 K. Concentric circles are separated by 0.04 K, $0.05f_0$, and 10^{-6} m/s for temperature, vorticity, and vertical velocity, respectively.

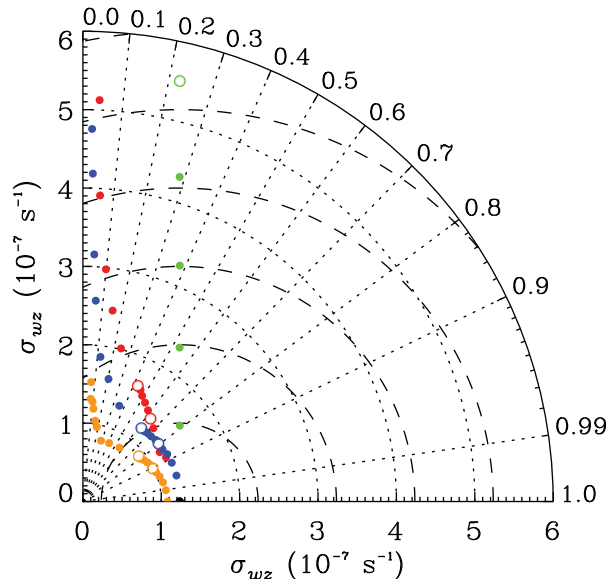


Figure 6. Taylor diagram for the fields shown in Figure 7 comparing noisy surface divergences (green), wavelet-denoised divergences (red), curvelet-denoised divergences (blue), and surface divergences derived from curvelet-denoised SST with a partial filtering with $\lambda_c = 30$ km (brown) with the fields without noise. Noise amplitude increases as the distance to the reference point (black bullet) increases. Circles correspond to the experiments with $\sigma_\epsilon = 0.05$ K and $\sigma_\epsilon = 0.1$ K reported in Table 2. Bullets corresponds to experiments with noise amplitudes increasing by 0.01 K for the range between 0 and 0.1 K and by 0.1 K between 0.1 and 1 K. Concentric circles are separated by 10^{-7} s^{-1} .

adopted only takes into account the signal-to-noise ratio to decide whether a coefficient could be affected by noise or not, consequently adapting automatically to a wide range of dynamical regions and noise levels. On the contrary, low-pass filters remove all signals at scales shorter than a cutoff frequency λ_c , imposing an external limit on the spatial resolution of the output field. Furthermore, the use of a low-pass filter in regions with a small signal-to-noise ratio does not correct the contribution of noise to larger scales, which can induce too shallow spectra.

[32] The wavelet-based multiresolution analysis here used to denoise SST fields has also been proposed to combine observations from different sensors with different spatial resolutions and noise levels [e.g., *Chin et al.*, 2013]. The underlining idea is based on the previous work by *Chin et al.* [1998] and consists in, first, project SST fields from different sensors onto a wavelet base. Then, use variational analysis to estimate the wavelet coefficient that minimizes a cost function for the given set of observations. And, finally, invert the wavelet transform. This algorithm also takes into account the noise level of the observations through the use of weights in the minimization procedure. Our results suggest two potential improvements to this algorithm. One based on the use of hard-thresholding (equation (11)) before computing the optimal wavelet coefficient. The other based on the use of different base functions, i.e., curvelets instead of isotropic wavelets.

[33] In this study we have used the SQG equations as a simplified model of the upper ocean to investigate the impact of noise when diagnosing ocean dynamics from satellite observations. Since we have used numerical simulations of SQG turbulence to perform the numerical experiment, our results are not affected by the validity of the SQG for the ocean. Nevertheless, the validity of our theoretical framework is a relevant question that naturally arises. During the last years several studies have addressed it through the analysis of spectral slopes of sea surface heights (SSHs) provided by altimeters [*Le Traon et al.*, 2008; *Xu and Fu*, 2011, 2012], showing that spectral slopes in the mesoscale band in highly energetic areas very closely follow the $k^{-11/3}$ slope coherent with a dominance of the SQG mode. In low-energy areas, altimetric noise makes difficult the determination of the spectral slopes [*Xu and Fu*, 2012], but the analysis of high-resolution numerical studies also suggest that spectral slopes are closer to the SQG mode in these areas [*Sasaki and Klein*, 2012]. Additional results were provided by *Kim et al.* [2011], who found spectral slopes equivalent to a SSH k^{-4} slope for scales smaller than 100 km from high-frequency radar observations just off the U.S. West Coast. In addition, several authors have shown that under the appropriate environmental conditions SQG equations can be used to diagnose ocean dynamics from satellite SST observations [*Isern-Fontanet et al.*, 2006a; *LaCasce and Mahadevan*, 2006], which provides its best results for energetic areas and deep ML [*Isern-Fontanet et al.*, 2008; *Lapeyre*, 2009]. Such results were consistent with the spreading of surface drifters in the North Atlantic [*Lumpkin and Elipot*, 2010]. It is worth mentioning that *LaCasce and Mahadevan* [2006] also investigated the diagnosis of the 3-D dynamics in Alboran area using the SQG equations. In particular, they diagnosed ocean dynamics using satellite SST measurements, which were smoothed using a Laplacian filter, and compared the results with the analyzed fields derived from in situ measurements during 3 day long surveys. Their results revealed significant differences between the fields derived from satellite observations and in situ measurements, which in our opinion were related to the lack of synopticity of in situ measurements.

[34] The application of equations (1–5) requires the estimation of three parameters: n_0 , n_e , and α' . The first parameter n_0 is related to the mean Brunt-Väisälä frequency N_0 and can be estimated from climatologies or if they are available, from ARGO observations. The quotient $\alpha' n_e^{-1}$ sets the energy level in equation (1) and can be determined from altimetric measurements as proposed in *Isern-Fontanet et al.* [2008]. The difficulty arises when one tries to determine the individual values of α' and n_e needed in equations (3) and (5). The simplest solution is to use in situ measurements to estimate α' , when available, or use existing realistic numerical simulations in the area [e.g., *Isern-Fontanet et al.*, 2008]. If such information is not available, only the topology of the upwelling/downwelling patterns can be investigated. This situation reinforces the idea of using the partial filtering approach proposed here to reduce the presence of spurious patches.

[35] An important question that remains open is the validation of fields such as vertical velocities and surface divergence diagnosed from real infrared observations. Due to

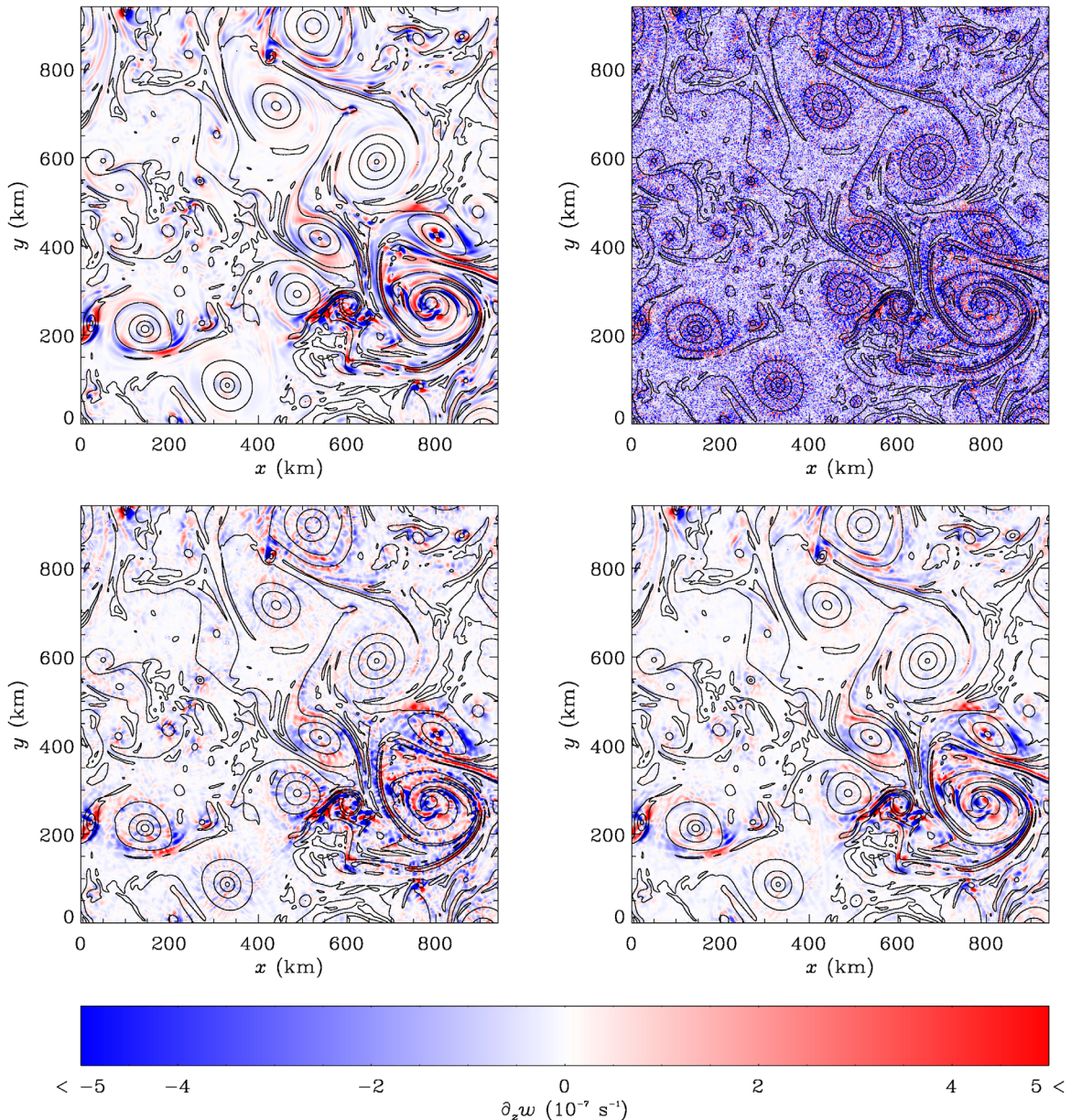


Figure 7. (top to bottom and left to right) Zoom of the original surface divergence obtained from numerical simulations of SQG turbulence; surface divergence calculated from SST with noise; surface divergence from SST denoised using curvelets; and surface divergence from SST denoised using curvelets and a partial filtering with $\lambda_c = 30$ km. The noise level used in the three experiment shown was $\sigma_\epsilon = 0.1\text{K}$. Black lines correspond to the original SST contours.

the strong impact of vertical fluxes on phytoplankton, one may be tempted to do it comparing chlorophyll concentration and upwelling/downwelling patterns. This idea is reinforced by the example shown in Figure 8, where there is a good co-location of strong upwelling and high chlorophyll concentrations. However, our approach is not able to capture all sources of vertical velocity in the ocean nor takes into account horizontal advection [e.g., Klein *et al.*, 2009; Levy *et al.*, 2012], implying that chlorophyll distribution may be quite different from the diagnosed vertical velocities. On the contrary, the capability to diagnose its low-frequency component can contribute to better understand

some aspects of the coupling between physics and biology. Nevertheless, the capability to retrieve vertical velocities from real SST satellite observations opens the door to a validation with in situ measurements, if good simultaneous data sets can be found.

[36] The denoising of ocean satellite images can still be improved through, at least, three different strategies that should be explored in future studies. First, one could use basis functions that may be even better adapted to the topology of the underlying flow. Some candidate could be the anisotropic wavelets or the contourlets proposed by Do and Vetterli [2005] and Cunha *et al.* [2006]. Second, one

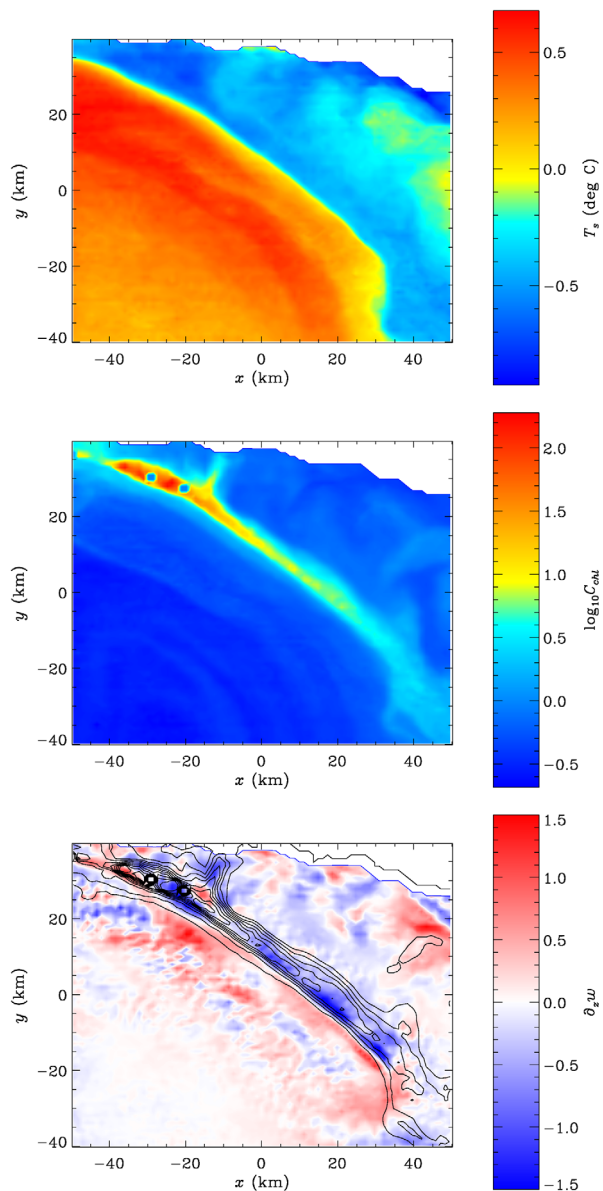


Figure 8. (top to bottom) BT image denoised using curvelets; simultaneous chlorophyll concentration; and surface divergence estimated using the partial filtering strategy from the BT image with the chlorophyll concentration overplotted. The image was provided by the MODIS-Aqua sensor on 24 March 2008 in the Alboran sea (western Mediterranean).

could improve the criterion used to modify the coefficients of the base functions. A common alternative to hard-thresholding (equation (11)) is to use *soft thresholding*, defined as

$$b_m = \begin{cases} \text{sign}(a_m)(|a_m| - \tau_m) & \text{if } |a_m| > \tau_m \\ 0 & \text{if } |a_m| \leq \tau_m \end{cases}, \quad (16)$$

which has the advantage of providing smoother fields but at the price of reducing the overall energy. Another alternative that could be explored would be the use of variational

analysis as in *Chin et al. [1998]*. Third, one could consider a combined method that uses both wavelet and curvelets [*Starck and Murtagh, 2006*]. This approach could represent a significant improvement since a turbulent flow is composed by vortices, well approximated by isotropic wavelets, and filaments, well approximated by curvelets.

[37] Finally, equations (1–3) can be written in terms of SSH [*Isern-Fontanet et al., 2008; Klein et al., 2009*], and the method here proposed can be directly applied to the future measurements that will be provided by the Surface Water and Ocean Topography (SWOT) mission. It is worth mentioning that the methodology proposed in this paper is not tied to the validity of the SQG approach. Indeed, any observed variable such as SST, SSH, or ocean color that has to be manipulated to extract quantitative information will benefit from the denoising strategies here proposed, e.g., the estimation of vorticity from the future high-resolution SSH measurements. Furthermore, one can notice that the denoising can also be applied to vorticity diagnosed from noisy SST and then reconstruct the original SST. This would allow to isolate the contribution of the different dynamical patterns as in *Isern-Fontanet et al. [2006b]*.

6. Conclusions

[38] The noise present in infrared sensors limits its use to diagnose dynamical fields at submesoscales. In this study, we have shown that the contribution of noise at scales of the order of a few kilometers can be significantly reduced by the use of the curvelet denoising approach together with the partial filtering strategy applied to the diagnosis of divergence. Our results open the door to systematic estimates of vorticity, vertical velocities, and surface divergence from existing infrared observations, which should help to better understand physical-biological interactions and the contribution of these scales to vertical fluxes in the ocean. Furthermore, the method is general and can be applied to remove noise from a wide range of remote observations such as ocean color or the future high-resolution SSH measurements of SWOT.

[39] **Acknowledgments.** This study is a contribution to the MED3D project funded by the Spanish R+D+i Plan (CTM2009–11020). J.I.-F. is funded through a Ramon y Cajal contract. We would like to thank Bertrand Chapron for stimulating discussions during the initial phases of this study. We would also like to thank Marcos Portabella and Isabel Andreu-Burillo for their useful comments.

References

- Bowen, M., J. Eney, P. Wilkin, P. Tildesley, I. Barton, and R. Knewston (2002), Extracting multilayer surface currents from sequential thermal imagery using the maximum cross-correlation technique, *J. Atmos. Oceanic Technol.*, 19, 1665–1676.
- Brown, O., and P. Minnett (1999), MODIS infrared sea surface temperature algorithm theoretical basis document version 2.0, technical report, Univ. of Miami. http://modis.gsfc.nasa.gov/data/atbd/atbd_mod25.pdf.
- Buades, A., B. Coll, and J. Morel (2010), Image denoising methods. A new nonlocal principle?, *SIAM Rev.*, 1, 113–147.
- Candès, E., L. Demanet, D. Donoho, and L. Ying (2006), Fast discrete curvelet transforms, *Multiscale Model. Simul.*, 5(3), 861–899.
- Capet, X., P. Klein, B. Hua, G. Lapeyre, and J. McWilliams (2008), Surface kinetic energy transfer in surface quasi-geostrophic flows, *J. Fluid Mech.*, 604, 165–174.
- Chang, S., B. Yu, and M. Vetterli (2000), Adaptive wavelet thresholding for image denoising and compression, *IEEE Trans. Image Process.*, 9(9), 1532–1546.

- Chin, T., R. Milliff, and W. Large (1998), Basin-scale, high-wavenumber sea surface wind fields from a multiresolution analysis of scatterometer data, *J. Atmos. Oceanic Technol.*, *15*(3), 741–763, doi:10.1175/1520-0426(1998)015<0741:BSHWSS>2.0.CO;2.
- Chin, T., J. Vazquez, and E. Armstrong (2013), Algorithm theoretical basis document: A multi-scale, high-resolution analysis of global sea surface temperature, technical report, version 1.1, Jet Propul. Lab., NASA. [Available at ftp://mariana.jpl.nasa.gov/mur_sst/tmchin/docs/ATBD/atbd_1.1.pdf].
- Cunha, A., J. Zhou, and M. Do (2006), The nonsubsampling contourlet transform: Theory, design, and applications, *IEEE Trans. Image Process.*, *15*(10), 3089–3101.
- Do, M., and M. Vetterli (2005), The contourlet transform: an efficient directional multiresolution image representation, *IEEE Trans. Image Process.*, *14*(12), 2091–2106.
- Donoho, D., and I. Johnston (1994), Ideal spatial adaptation by wavelet shrinkage, *Biometrika*, *81*(3), 425–455.
- Ferrari, R. (2011), A frontal challenge for climate models, *Science*, *332*, 316–317, doi:10.1126/science.1203632.
- Held, I., R. Pierrehumbert, S. Garner, and K. Swanson (1995), Surface quasi-geostrophic dynamics, *J. Fluid Mech.*, *282*, 1–20.
- Isern-Fontanet, J., B. Chapron, P. Klein, and G. Lapeyre (2006a), Potential use of microwave SST for the estimation of surface ocean currents, *Geophys. Res. Lett.*, *33*, L24608, doi:10.1029/2006GL027801.
- Isern-Fontanet, J., E. García-Ladona, J. Font, and A. García-Olivares (2006b), Non-Gaussian velocity probability density functions: An altimetric perspective of the Mediterranean sea, *J. Phys. Oceanogr.*, *36*(11), 2153–2164.
- Isern-Fontanet, J., G. Lapeyre, P. Klein, B. Chapron, and M. Hetcht (2008), Three-dimensional reconstruction of oceanic mesoscale currents from surface information, *J. Geophys. Res.*, *113*, C09005, doi:10.1029/2007JC004692.
- Kim, S., et al. (2011), Mapping the U.S. West Coast surface circulation: A multiyear analysis of high-frequency radar observations, *J. Geophys. Res.*, *116*, C03011, doi:10.1029/2010JC006669.
- Klein, P., and L. Lapeyre (2009), The oceanic vertical pump induced by mesoscale and submesoscale turbulence, *Annu. Rev. Mar. Sci.*, *1*, 351–375, doi:10.1146/annurev.marine.010908.163704.
- Klein, P., J. Isern-Fontanet, G. Lapeyre, G. Roullet, E. Danioux, B. Chapron, S. Le Gentil, and H. Sasaki (2009), Diagnosis of vertical velocities in the upper ocean from high resolution sea surface height, *Geophys. Res. Lett.*, *33*, L24608, doi:10.1029/2009GL038359.
- LaCasce, J., and A. Mahadevan (2006), Estimating subsurface horizontal and vertical velocities from sea surface temperature, *J. Mar. Res.*, *64*, 695–721.
- Lapeyre, G. (2009), What mesoscale signal does the altimeter see? On the decomposition in baroclinic modes and the role of the surface boundary condition, *J. Phys. Oceanogr.*, *39*, 2857–2874.
- Lapeyre, G., and P. Klein (2006), Dynamics of the upper oceanic layers in terms of surface quasigeostrophy theory, *J. Phys. Oceanogr.*, *36*, 165–176.
- Le Traon, P., P. Klein, B. Hua, and G. Dibarboure (2008), Do altimeter wavenumber spectra agree with interior or surface quasi-geostrophic theory?, *J. Phys. Oceanogr.*, *38*, 1137–1142.
- Levy, M., R. Ferrari, P. Franks, A. Martin, and P. Riviere (2012), Bringing physics to life at the submesoscale, *Geophys. Res. Lett.*, *39*, L14602, doi:10.1029/2012GL052756.
- Lumpkin, R., and S. Elipot (2010), Surface drifter pair spreading in the North Atlantic, *J. Geophys. Res.*, *115*, C12017, doi:10.1029/2010JC006338.
- Mallat, S. (1999), *A Wavelet Tour of Signal Processing*, Academic Press, San Diego, Calif.
- Robinson, I. (2004), *Measuring the Oceans From Space: The Principles and Methods of Satellite Oceanography*, 669 pp., Springer/Praxis.
- Sasaki, H., and P. Klein (2012), SSH wavenumber spectra in the north pacific from a high-resolution realistic simulation, *J. Phys. Oceanogr.*, *42*, 1233–1241.
- Schneider, K., and M. Farge (2006), Wavelets: Mathematical theory, in *Encyclopedia of Mathematical Physics*, pp. 426–438, Academic Press, San Diego, Calif., doi:10.1016/B0-12-512666-2/00153-X.
- Starck, J., and F. Murtagh (2006), *Astronomical Image and Data Analysis*, Springer-Verlag, Berlin, Germany.
- Starck, J., E. Candès, and D. Donoho (2002), The curvelet transform for image denoising, *IEEE Trans. Image Process.*, *11*(6), 670–684.
- Taylor, K. (2001), Summarizing multiple aspects of model performance in a single diagram, *J. Geophys. Res.*, *106*, 7183–7192, doi:10.1029/2000JD900719.
- Turiel, A., J. Isern-Fontanet, and E. García-Ladona (2007), Wavelet filtering to extract coherent vortices from altimetric data, *J. Atmos. Oceanic Technol.*, *24*(12), 2103–2119.
- Xu, Y., and L. Fu (2011), Global variability of the wavenumber spectrum of oceanic mesoscale turbulence, *J. Phys. Oceanogr.*, *41*, 802–809.
- Xu, Y., and L. Fu (2012), The effects of altimeter instrument noise on the estimation of the wavenumber spectrum of sea surface height, *J. Phys. Oceanogr.*, *42*(12), 2229–2233, doi:10.1175/JPO-D-12-0106.1.